ACCELERON AEROSPACE JOURNAL (AAJ)
E-ISSN: 2583-9942 (Online) | Accessible at www.acceleron.org.in
Volume 5, Issue 1, (pp.1281-1295)
Article ID: AAJ.11.2106-2542
Research Paper
https://doi.org/10.61359/11.2106-2542

CFD-Based Analysis of Divergent Section Deflection for Thrust Vector Control in 2D Nozzles

Durkhanay Banuri*, Asad Ahsan†

Institute of Space Technology, Islamabad, Pakistan.

Abstract: This study presents a computational fluid dynamics (CFD) analysis of thrust vector control (TVC) through mechanical deflection of the divergent section in a 2D convergent-divergent nozzle. Using CATIA, three nozzle configurations with deflection angles of 15°, 20°, and 25° were designed and simulated in ANSYS Fluent under identical boundary conditions. Air was modeled as an ideal gas with temperature-dependent viscosity, and the simulations employed a density-based, steady-state solver with the SST k-ω turbulence model. High-resolution unstructured meshing with wall inflation layers ensured accurate capture of near-wall effects, flow separation, and shock formations. The results reveal how variations in divergent geometry influence internal flow characteristics, including Mach number, pressure distribution, temperature gradients, and mass flow rate. Particular attention was given to the generation and interaction of oblique shock waves at higher deflection angles. The findings provide insight into nozzle performance, thrust deviation, and shock-induced flow asymmetries, contributing to more effective TVC system design in aerospace applications.

Table of Contents

1. Introduction

Thrust vectoring (TVC) is a propulsion control technique that enables redirection of engine thrust, offering enhanced maneuverability in flight regimes where traditional aerodynamic surfaces lose effectiveness. It plays a vital role in advanced aircraft, launch vehicles, and next-generation UAVs, particularly during high-angle-of-attack flights, post-stall conditions, or atmospheric transition phases. While extensive research exists on TVC using axisymmetric or gimbaled nozzle deflections, fewer studies have explored the aerodynamic implications of varying the divergent section geometry itself. This study investigates the aerodynamic effects of mechanically altering the divergent angles in a 2D convergent-divergent (C-D) nozzle as a means of implementing thrust vector control. Rather than deflecting the entire nozzle assembly, the focus is on evaluating how different divergent deflection angles influence internal flow behavior, including Mach number, pressure distribution, temperature, and mass flow rate. The nozzle configurations are designed parametrically in CATIA and simulated using ANSYS Fluent under consistent boundary conditions. This approach enables a controlled, high-fidelity comparison of flow characteristics across divergent angles of 5°, 7°, 9°, and 11°, under deflection conditions of 15°, 20°, and 25°, contributing new insight into the role of divergent geometry in nozzle-based thrust vectoring systems.

2. Methodology

The nozzle geometries (Appendix-A) used in this study were developed using CATIA V5, focusing on three deflection angles 15°, 20°, and 25° with consistent inlet and throat dimensions across all cases to isolate the effect of divergent angle variation. CATIA's parametric modeling environment enabled accurate shaping and smooth curvature transitions essential for realistic flow behavior. The final geometries were exported in STEP format to retain dimensional fidelity for downstream CFD analysis.

*Institute of Space Technology, Islamabad, Pakistan.
†Institute of Space Technology, Islamabad, Pakistan. **Corresponding Author:** asadahsan716@gmail.com.
Article History: Received: 16-July-2025 || Revised: 27-July-2025 || Accepted: 30-July-2025 || Published Online: 30-July-2025.

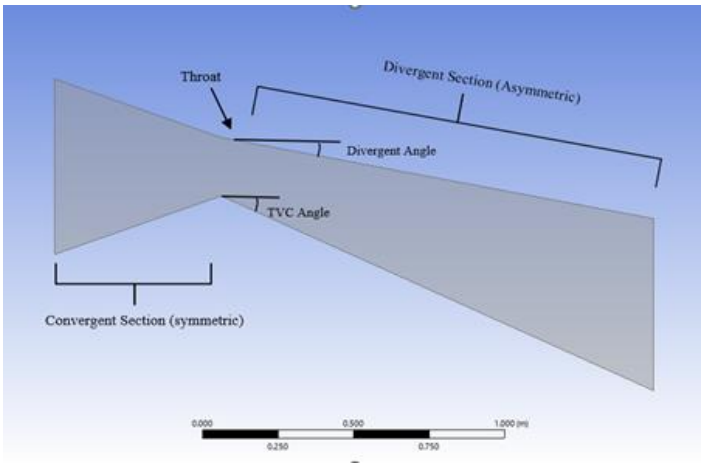

Figure 1: Nozzle Geometry

Figure 1 illustrates the nozzle geometry consisting of a symmetric convergent section with a fixed 20° angle and 600 mm inlet length. The throat is maintained at 200 mm. The divergent and thrust vector control (TVC) sections extend 1450 mm and have variable angles, resulting in an asymmetric overall profile.

The geometries were imported into ANSYS Fluent, where preprocessing involved domain setup, boundary definition, and mesh generation. A two-dimensional axisymmetric approach was adopted to reduce computational cost while preserving key internal flow physics. The computational domain was defined as a velocity inlet, a pressure outlet, and adiabatic no-slip wall boundaries. Titanium was assigned as the wall material. The operating pressure was set to 0 Pa, and all simulations were conducted at 300 K using air modeled as an ideal gas, with temperature-dependent viscosity governed by Sutherland's law.

Figure 2 hows the unstructured mesh generated using ANSYS Meshing, with local refinement applied in critical regions such as the throat, wall boundaries, and nozzle exit. A base element size of 5 mm was used with a growth rate of 1.05 to maintain mesh smoothness and numerical stability. Inflation layers were implemented along all solid boundaries to resolve near-wall gradients, targeting a dimensionless wall distance (Y^+) below 1. Quality metrics, including skewness and orthogonality, were monitored throughout the process. Refinement zones were introduced near areas expected to exhibit strong gradients or potential flow separation to enhance solution accuracy.

Simulations were performed using ANSYS Fluent's density-based solver in double precision, under steady-state conditions with the energy equation activated. The SST k-ω turbulence model was selected for its robustness in predicting boundary layer behavior and flow separation. Enhanced wall treatment was employed to enable the solver to adapt between low-Re and wall-function approaches as needed. Solver settings included implicit formulation for pressure-velocity coupling and second-order upwind discretization schemes for spatial gradients. Standard initialization was applied from the inlet, and up to 2500 iterations were allowed per case, with convergence defined by residuals dropping below 1×10^{-5}. Velocity and pressure monitors were placed at the

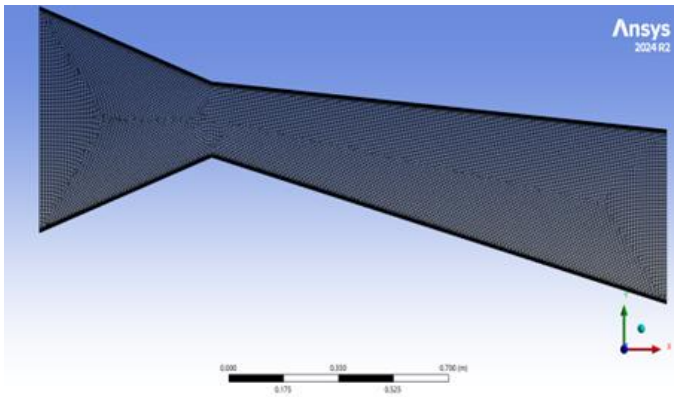

Figure 2: Nozzle Mesh

nozzle exit to ensure physical convergence alongside numerical criteria. The governing momentum equation, incorporating turbulence effects via the SST k–ω model, is given by:

Acceleron Aerospace Journal || AAJ.11.2106-2542
Volume 5, Issue 1, pp (1281-1295)
E-ISSN- 2583-9942
https://dx.doi.org/10.61359/11.2106-2542

$$\rho(v \cdot \nabla)v = -\nabla p + \nabla \cdot [(\mu + \mu_t)(\nabla v + (\nabla v)^T)]$$

Where ρ is the fluid density, v is the velocity vector, p is the static pressure, μ is the molecular dynamic viscosity, and μ_t is the turbulence-induced eddy viscosity computed from the SST k–ω model. This equation balances the convective acceleration on the left with pressure gradients and combined molecular and turbulent viscous stresses on the right, capturing the key physics of compressible, viscous flow through the nozzle.

Post-processing was conducted within Fluent and included extraction of velocity vectors, Mach number distributions, pressure and temperature contours, streamlines, and mass flow rates. These outputs facilitated a comparative analysis of each configuration, with particular attention to jet deflection angles, pressure asymmetries, flow separation zones, and thrust direction deviation. Results were used to assess how variations in divergent section geometry influence overall nozzle performance and thrust vectoring behavior under consistent operating conditions.

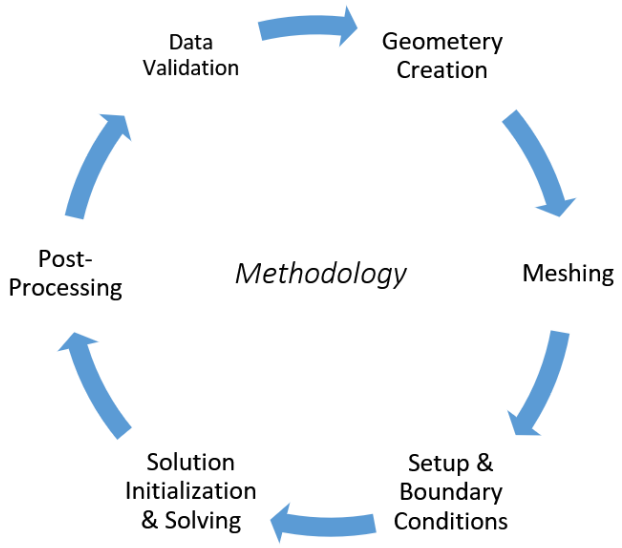

Figure 3: Analysis Process

Figure -3 presents the iterative CFD analysis workflow used in this study. It starts with geometry creation, followed by meshing with appropriate refinement. The setup phase includes defining boundary conditions and solver settings, leading to the solution stage where the simulation runs. In post-processing, key flow and performance data are extracted. Based on the results, adjustments may be made, repeating the cycle for improved accuracy.

3. Ansys Fluent Analysis

Twelve nozzle geometries were created in CATIA V5 by combining three deflection angles (15°, 20°, 25°) with four divergent angles (5°, 7°, 9°, 11°). Each design featured a constant throat diameter, with the divergent section modified to induce thrust deflection. 2D sketches were revolved into 3D solids, ensuring smooth curvature for realistic flow behavior. Models were exported as STEP files for CFD analysis.

Table 1: Mesh Results

Nodes	47781
Elements	46034

In ANSYS Meshing, unstructured tetrahedral grids were generated with five inflation layers near the walls to capture boundary layers. A growth rate of 1.05 and $y^+ \approx 1$ were maintained to support the SST k-ω turbulence

model. Consistent named selections were applied across all geometries. The final mesh resulted out as mentioned in Table 1.

4. Mesh Independence Test

A mesh independence study (Table-2) confirmed convergence at mesh sizes ≤ 6 mm. The final 5 mm mesh (47,781 nodes, 46,034 elements) provided accurate results with acceptable computational cost. Mach number variations across mesh sizes remained within 2%, validating mesh quality and consistency.

Table 2: Mesh Independence Study

Mesh size (mm)	Nodes	Elements	Mach no.
3	80329	77620	2.3721
4	60020	57880	2.3700
5	47781	46034	2.3685
6	38210	36500	2.3671
7	31000	29500	2.3664
8	25500	24300	2.3660

5. Discussion

The simulation was performed using a density-based implicit solver with second-order upwind schemes, suitable for high-speed compressible nozzle flows. A 2D steady-state setup was used to reduce computational cost while capturing key flow characteristics. The SST k-ω turbulence model was chosen for its accuracy in handling boundary layers and shock interactions.

Air (ideal gas) was used as the working fluid. The inlet was defined as a pressure inlet with a total gauge pressure of 1.8 MPa and a temperature of 300 K, while the outlet was set as a pressure outlet at 0.2 MPa. This configuration ensures a strong pressure gradient for flow acceleration.

Standard initialization from the inlet was applied, and key flow parameters, including Mach number, static pressure, mass flow rate, and outlet temperature, were monitored for performance evaluation.

A summary of all setup parameters is provided in (Table-3)

Table 3: Boundary Conditions and Solver Summary

Parameter	Value / Description
Solver Type	Density-Based (Implicit, 2nd Order Upwind)
Simulation Type	2D Steady-State
Turbulence Model	SST k-ω (Shear Stress Transport)
Fluid Model	Air (Ideal Gas)
Operating Pressure	0 Pa
Inlet Boundary Condition	Pressure Inlet

Acceleron Aerospace Journal || AAJ.11.2106-2542
Volume 5, Issue 1, pp (1281-1295)
E-ISSN- 2583-9942
https://dx.doi.org/10.61359/11.2106-2542

Total Gauge Pressure	1,800,000 Pa
Initial Gauge Pressure	800,000 Pa
Temperature	300 K
Outlet Boundary Condition	Pressure Outlet
Gauge Pressure	200,000 Pa
Temperature	300 K
Initialization	Standard Initialization from Inlet
Monitors Set For	Mach Number, Static Pressure, Mass Flow Rate, Temperature at Outlet

6. Results and Analysis

Pressure Contours

Pressure gradients increase near the curved inner wall of the nozzle, causing asymmetric loading and thus contributing to lateral force generation. As deflection (D# TV#) increase, stagnation pressure on one side of the nozzle becomes more dominant.

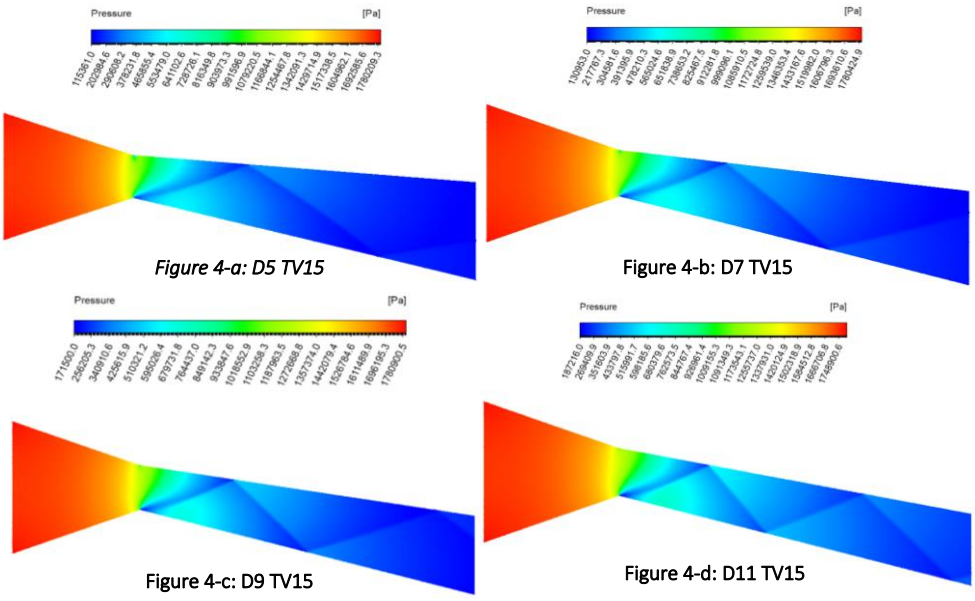

Figure 4-a: D5 TV15

Figure 4-b: D7 TV15

Figure 4-c: D9 TV15

Figure 4-d: D11 TV15

Figure 4: Pressure Contour with 15 deg TV Deflection

Figure 4 presents the pressure contours for nozzle configurations D5 to D11 at a fixed 15° thrust vector (TV) deflection. In D5 (Figure 4-a), the pressure drop is smooth and symmetric along the divergent section, indicating stable supersonic flow. As the divergence increases in D7 (Figure 4-b) and D9 (Figure 4-c), slight pressure asymmetry appears along the upper and lower walls due to the angled geometry, leading to the formation of mild pressure gradients. In D11 (Figure 4-d), more pronounced pressure variation is observed, especially near the wall regions, where internal shock structures begin to develop. However, the flow remains fully attached and there is no evidence of expansion fans or separation. Overall, increasing divergence at constant TV deflection modifies the internal pressure distribution, influencing the direction and intensity of thrust vectoring.

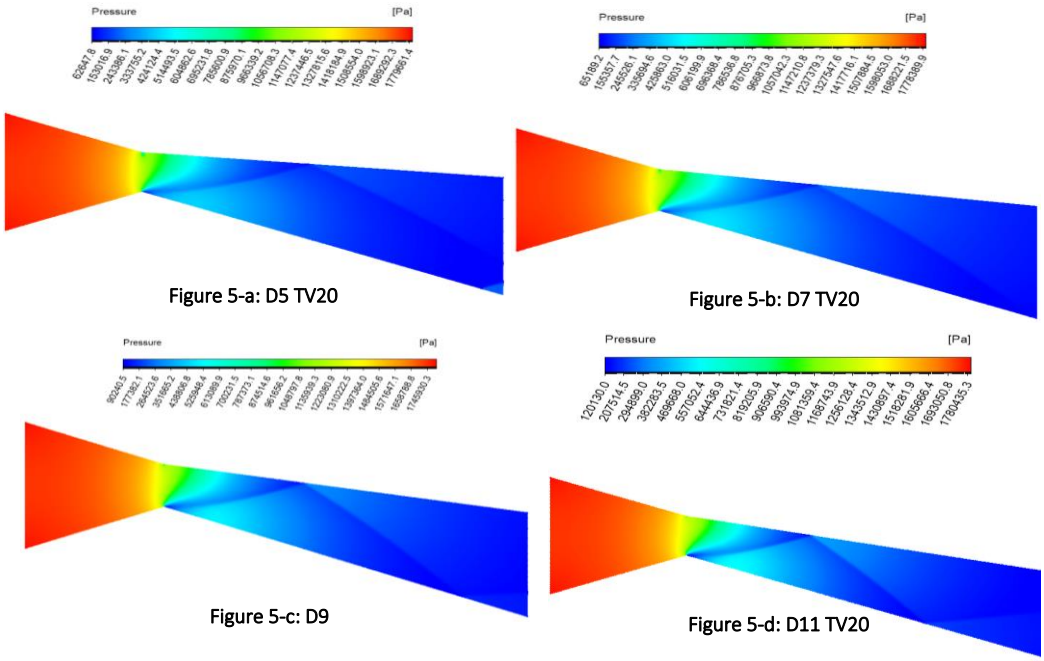

Figure 5: Pressure Contour with 20 deg TV Deflection

Figure 5 displays the pressure contours for nozzle configurations D5 to D11 at a fixed 20° TV deflection. Compared to the 15° case, the pressure drop across the divergent section becomes steeper, and wall pressure asymmetry becomes more pronounced due to the increased deflection angle. In D5 (Figure 5-a) and D7 (Figure 5-b), the pressure gradients remain relatively smooth, with slight compression visible near the upper wall, indicating early internal pressure imbalance. D9 (Figure 5-c) shows more distinct localized pressure increases, suggesting the formation of mild oblique shock structures. In D11 (Figure 5-d), the pressure field becomes increasingly asymmetric, with denser high-pressure zones forming near the lower wall, indicating stronger internal compression. These results demonstrate that at higher TV angles, the effect of divergent geometry on internal pressure distribution is amplified, influencing the strength and directionality of the resulting thrust vector.

Figure 6 presents the pressure contours for nozzle configurations D5 to D11 at a 25° TV deflection, the highest tested angle. The internal pressure field shows clear intensification of wall pressure gradients and localized compression zones across all cases. In D5 (Figure 6-a) and D7 (Figure 6-b), pressure remains mostly well-distributed, but asymmetry becomes more evident along the divergent walls. D9 (Figure 6-c) exhibits localized high-pressure patches near the lower wall, indicative of stronger shock development compared to previous deflections. In D11 (Figure 6-d), these effects are amplified, with high-pressure zones dominating the lower portion of the nozzle, suggesting concentrated internal compression. While no clear shock reflections or separations are visible, the increasingly distorted pressure field confirms that higher deflection angles, when combined with large divergent geometries, significantly alter the internal flow balance and strengthen thrust vectoring effects.

Acceleron Aerospace Journal || AAJ.11.2106-2542
Volume 5, Issue 1, pp (1281-1295)
E-ISSN- 2583-9942
https://dx.doi.org/10.61359/11.2106-2542

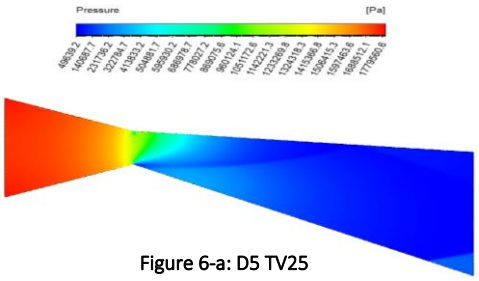

Figure 6-a: D5 TV25

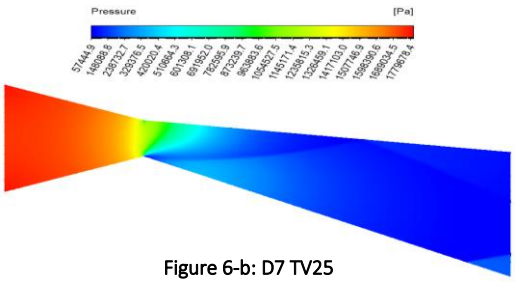

Figure 6-b: D7 TV25

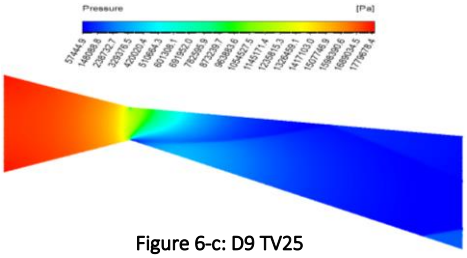

Figure 6-c: D9 TV25

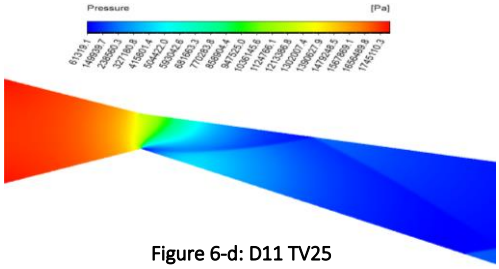

Figure 6-d: D11 TV25

Figure 6: Pressure Contour with 25 deg TV Deflection

Velocity Distribution

The velocity distribution inside the nozzle shows how the flow accelerates and redirects with the angle deflection. Compared to the baseline degree, flow deviation increases, showing evident curvature and high-speed stream redirection toward the intended vector.

Figure 7 shows the Mach number contours for nozzle configurations D5 to D11 at a fixed 15° TV deflection. In D5 (Figure 7-a), the supersonic core expands uniformly along the nozzle axis, maintaining a symmetrical profile with minimal lateral deviation. As the divergent angle increases in D7 (Figure 7-b) and D9 (Figure 7-c), the flow begins to redirect slightly toward the lower wall, indicating the onset of thrust vectoring. D11 (Figure 7-d) exhibits the most noticeable deviation, with the high-speed jet core tilted further downward and compressed near the lower boundary, confirming increased directional thrust. Despite these changes, the flow remains continuous and fully choked at the throat for all cases, with no signs of shock disruption or separation. This set demonstrates how increasing divergence at a fixed TV deflection gradually enhances flow turning and vectoring control without compromising supersonic expansion.

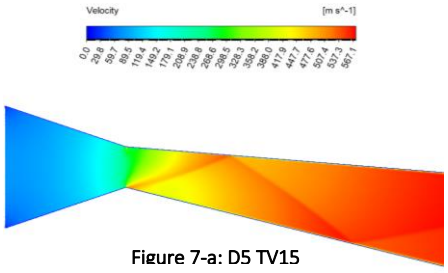

Figure 7-a: D5 TV15

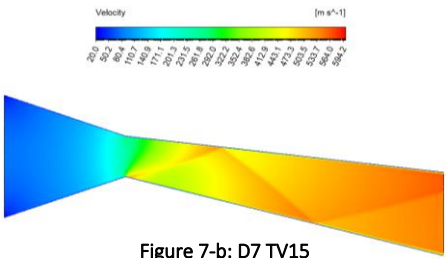

Figure 7-b: D7 TV15

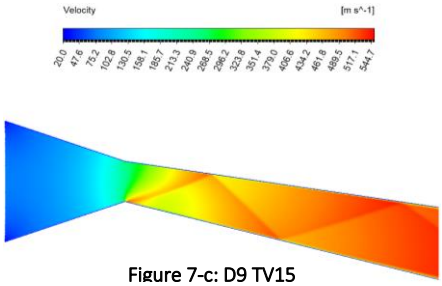

Figure 7-c: D9 TV15

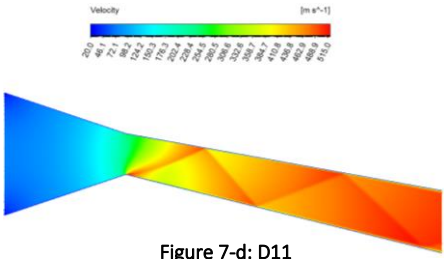

Figure 7-d: D11

Figure 7: Velocity Distribution with 15 deg TV Deflection

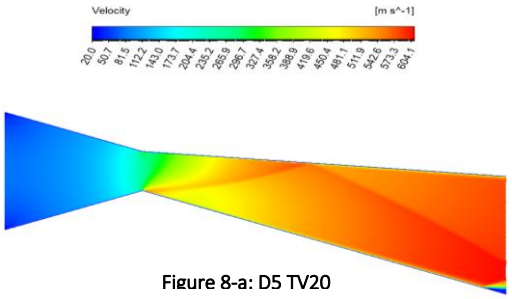

Figure 8-a: D5 TV20

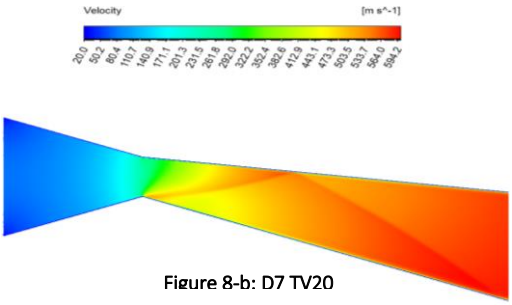

Figure 8-b: D7 TV20

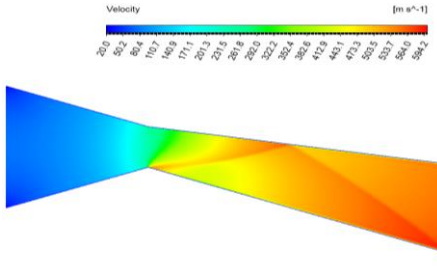

Figure 8-c: D9 TV20

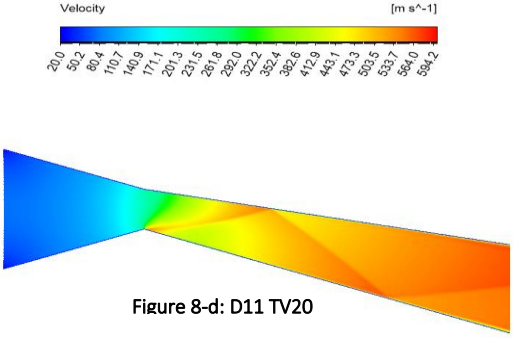

Figure 8-d: D11 TV20

Figure 8: Velocity Distribution with 20 deg TV Deflection

Figure 8 presents the Mach number contours for nozzle configurations D5 to D11 at a constant 20° TV deflection. Compared to the 15° case, a more pronounced downward deflection of the supersonic jet core is visible across all geometries. In D5 (Figure 8-a) and D7 (Figure 8-b), the core flow accelerates smoothly past the throat and bends slightly toward the lower wall, indicating effective but moderate thrust redirection. D9 (Figure 8-c) reveals a stronger shift in flow direction, with a more compressed high-Mach region along the lower boundary. In D11 (Figure 8-d), the jet core is visibly skewed and narrower, indicating a sharper turn and more focused vectoring effect. The flow remains fully choked and attached in all cases, and no shock structures are observed within the divergent section. Overall, this set demonstrates that at 20° TV deflection, nozzle geometry has a direct impact on the degree and sharpness of flow redirection, enhancing thrust control precision.

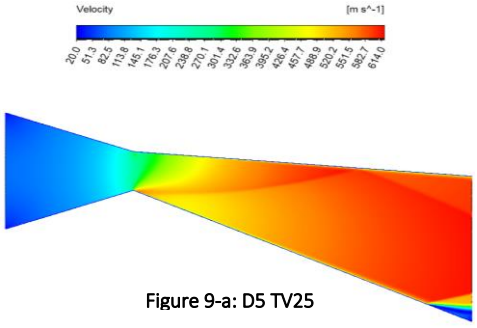

Figure 9-a: D5 TV25

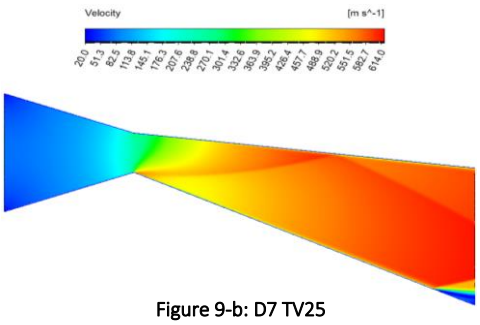

Figure 9-b: D7 TV25

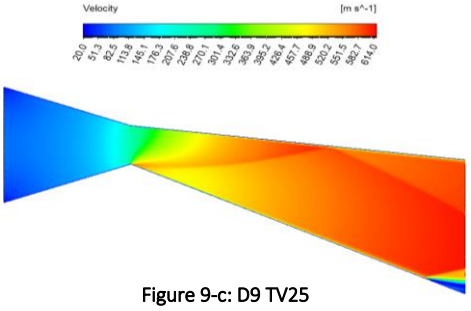

Figure 9-c: D9 TV25

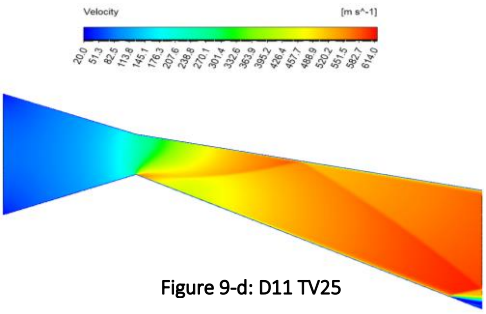

Figure 9-d: D11 TV25

Figure 9: Velocity Distribution with 25 deg TV Deflection

Figure 9 illustrates the velocity contours across nozzle configurations D5 TV25 to D11 TV25, clearly highlighting the effect of increased divergent angles under maximum thrust vectoring deflection. The flow accelerates smoothly

Acceleron Aerospace Journal || AAJ.11.2106-2542
Volume 5, Issue 1, pp (1281-1295)
E-ISSN- 2583-9942
https://dx.doi.org/10.61359/11.2106-2542

past the choked throat, reaching peak velocities near the lower wall due to asymmetric geometry-induced turning. As divergence grows from D5 (Figure 9 a) to D11 (Figure 9 d), the supersonic core increasingly bends downward, accompanied by localized deceleration zones and compressed streamlines that signal oblique shock development. Mild wall slip effects are observed along the divergent walls, while the inlet flow remains largely uniform. The highest divergence case (D11 TV25) shows a sharply skewed jet and thicker shear layer near the exit, indicating intensified flow redirection and shock–boundary layer interaction. Despite these disturbances, the flow remains choked at the throat, and no full separation occurs, confirming stable supersonic expansion but reduced exit Mach number due to internal shocks and enhanced pressure asymmetry.

Temperature Contours

Temperature distribution reveals localized heating along the nozzle walls, especially near regions of high compression and shock interaction. As deflection angle increases, thermal gradients become more pronounced due to asymmetric flow acceleration and pressure variation.

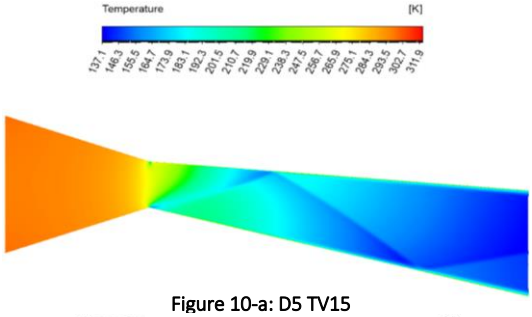

Figure 10-a: D5 TV15

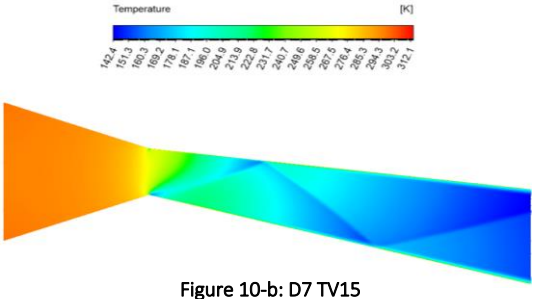

Figure 10-b: D7 TV15

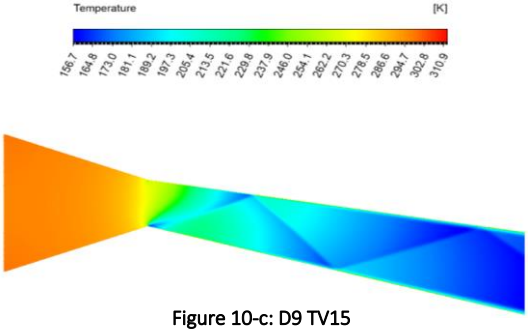

Figure 10-c: D9 TV15

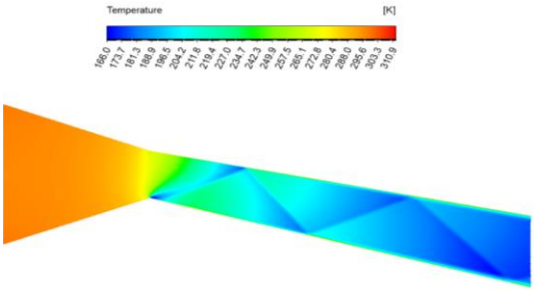

Figure 10-d: D11 TV15

Figure 10: Temperature Contour with 15 deg TV Deflection

Figure 10 presents the static temperature distribution for nozzle configurations D5 TV15 to D11 TV15, capturing the thermal response to moderate thrust vector deflection. After the choked throat, the core flow undergoes near-isentropic expansion in D5 (Figure 10 a), leading to uniformly lower temperatures along the divergent section. As the divergent angle increases through D7 and D9 (Figures 10 b and 10 c), localized wall heating appears near zones of mild compression, hinting at the onset of oblique shocks and wall slip effects. In D11 (Figure 10 d), these thermal gradients intensify, with visible hot streaks adjacent to the lower wall where flow turning is strongest. The asymmetric temperature field reflects combined effects of pressure imbalance, partial shock structures, and constrained expansion near the exit. Despite rising wall temperatures, the flow remains attached without separation, and the inlet temperature stays nearly constant, showing the balance between geometric deflection and thermodynamic efficiency at this lower TV angle.

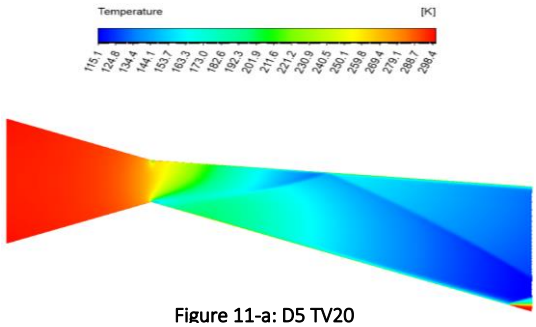

Figure 11-a: D5 TV20

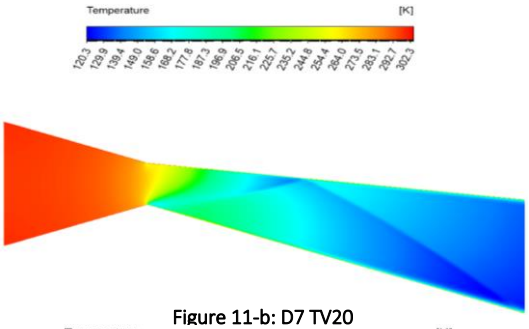

Figure 11-b: D7 TV20

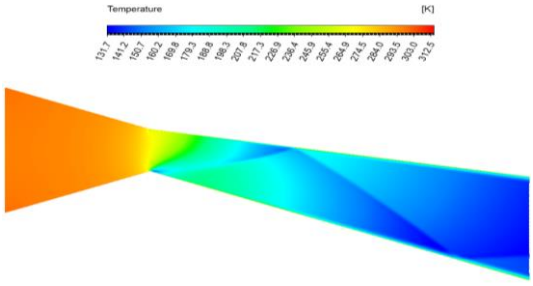

Figure 11-c: D9 TV20

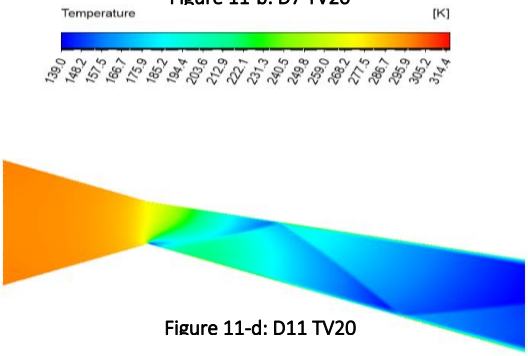

Figure 11-d: D11 TV20

Figure 11: Temperature Contour with 20 deg TV Deflection

Figure 11 depicts the temperature contours for configurations D5 TV20 to D11 TV20, highlighting the thermal impact of increased thrust vector deflection. Compared to the 15° case, the higher deflection intensifies asymmetric heating along the divergent walls, especially in D9 (Figure 11 c) and D11 (Figure 11 d), where oblique shock-induced recompression raises local static temperatures. Wall slip effects become more pronounced downstream, visible as concentrated hot regions near the lower boundary where the jet core bends sharply. In D5 and D7 (Figures 11-a and 11-b), the expansion remains relatively uniform with milder thermal gradients, but flow turning still causes slight temperature to rise near the exit. Throughout all cases, the flow remains choked at the throat, and while no large-scale separation is observed, the combination of higher divergent angles and deflection increases local wall heating and disrupts near-wall isentropic cooling, confirming a tradeoff between thrust vector sharpness and thermal uniformity.

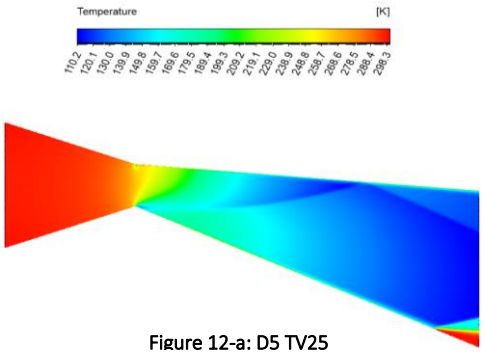

Figure 12-a: D5 TV25

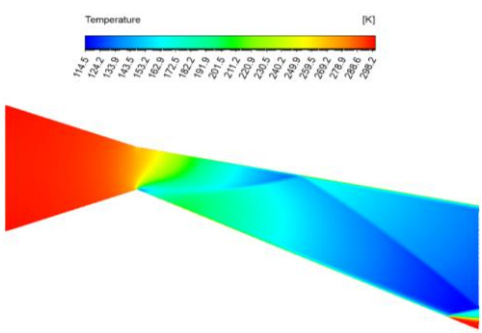

Figure 12-b: D9 TV25

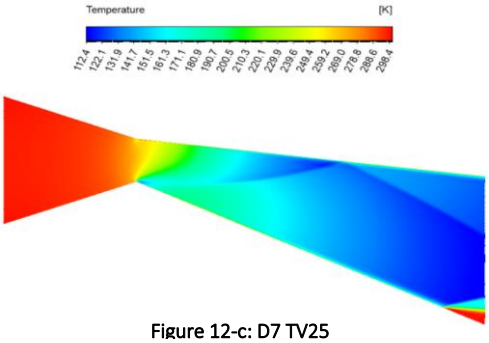

Figure 12-c: D7 TV25

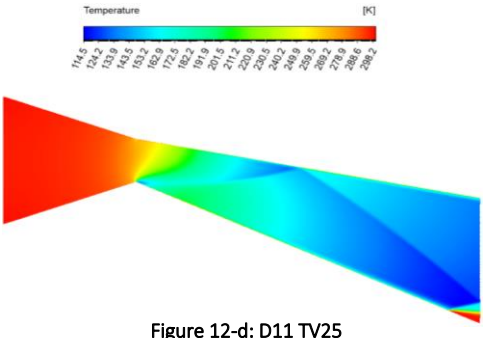

Figure 12-d: D11 TV25

Figure 12: Temperature Contour with 25 deg TV Deflection

Acceleron Aerospace Journal || AAJ.11.2106-2542
Volume 5, Issue 1, pp (1281-1295)
E-ISSN- 2583-9942
https://dx.doi.org/10.61359/11.2106-2542

Figure 12 shows the temperature contours for nozzle configurations D5 TV25 to D11 TV25, demonstrating the combined impact of maximum thrust vector deflection and divergent angle variation on thermal fields. In D5 (Figure 12 a) and D7 (Figure 12 c), the expansion initially maintains moderate cooling, but even here, localized heating appears near the lower divergent wall where the supersonic jet curves sharply. Moving to higher divergent angles in D9 (Figure 12 b) and especially D11 (Figure 12 d), pronounced hot zones emerge, driven by strong oblique shocks and intensified recompression downstream of the choked throat. These high-temperature regions align with flow turning and pressure asymmetry, while the inlet temperature stays unchanged at 300 K. Wall slip and boundary-layer thickening further distort thermal gradients near the nozzle exit, emphasizing how aggressive geometric deflection raises local static temperature and shock losses, subtly reducing isentropic efficiency yet sustaining controlled vectoring without large-scale separation.

7. Comparative Analysis

Table 4 Comparative Analysis of Results

Deflection	TV Control	Pressure [Pa]	Temperature [K]	Mach No.	Mass flow rate [kg/s]
5°	15°	131561.96	145.44	2.328	802.92
	20°	102130.75	140.78	2.416	808.53
	25°	87646.668	139.30	2.481	808.54
7°	15°	159118.66	153.67	2.203	796.11
	20°	110800	134.75	2.502	799.02
	25°	93726.762	141.76	2.430	801.67
9°	15°	200670.64	164.00	2.055	788.63
	20°	118659.78	141.75	2.387	788.25
	25°	102549.73	140.49	2.454	787.95
11°	15°	273080.39	179.11	1.852	780.86
	20°	140916.43	148.69	2.274	779.59
	25°	112706.18	149.08	2.288	784.30

Table 4 consolidates the CFD-predicted exit conditions across all nozzle configurations and thrust vector (TV) deflection angles, highlighting how divergent angle and deflection jointly shape flow behavior. As deflection increases from 15° to 25°, exit static pressure generally decreases at mild divergence (e.g., D5 TV25 ≈ 8.76×10^4 Pa) due to strong expansion fans, but rises sharply at larger divergence like D11 TV15 (≈ 2.73×10^5 Pa) from internal shock compression. The Mach number peaks at M≈2.50 for D7 TV20 where the geometry balances expansion length and moderate shock loss, then drops to M≈1.85 in D11 TV15 under severe overexpansion and shock train effects that thicken boundary layers and reduce exit velocity. Static temperature inversely follows lowest (≈139 K) where expansion is nearly isentropic, and highest (≈179 K) where shock-induced heating dominates. Mass flow rate varies modestly (≈780–810 kg/s), peaking in mid-deflection cases as optimal flow turning maintains throughput despite rising backpressure. Overall, the table quantifies the tradeoff between maximizing vector angle, preserving choked supersonic flow, and minimizing thermal and pressure penalties due to internal shocks and boundary layer interactions.

Figure 13 compares exit Mach numbers across all configurations, showing a clear trend where moderate divergent angles paired with mid-range TV deflection (notably D7 TV20) achieve the highest exit Mach ≈ 2.50, thanks to balanced expansion and minimal shock interference. At larger divergence and highest deflection (D11 TV25), exit Mach drops to ≈ 1.85 as internal oblique shocks and shock train effects disrupt the supersonic core and thicken the shear layer. The graph underlines how geometric deflection and divergent angle shape the degree of supersonic expansion and flow turning while sustaining choked flow at the throat.

Figure 14 shows that mass flow rate stays relatively stable across all cases, varying gently between ≈780–810 kg/s. Peak mass flux aligns with mid-deflection setups (e.g., D5 TV20 and D7 TV20), where efficient expansion offsets rising backpressure. At higher divergence or sharper vector angles, mass flow slightly drops as shock-induced boundary layer thickening and increased wall friction reduce throughput. Despite these shifts, choked flow at the throat ensures mass flow rate remains largely governed by inlet conditions and area geometry.

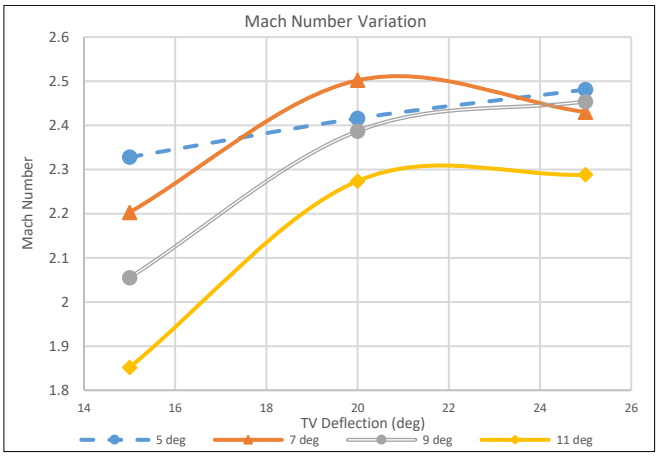

Figure 13: Mach Comparison

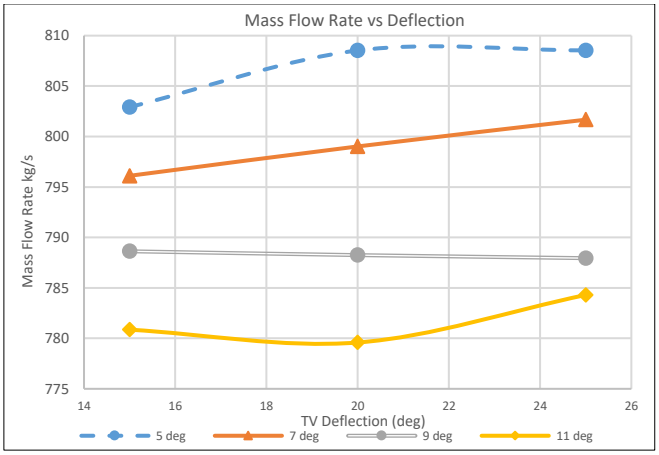

Figure14: Mass Flow Rate Comparison

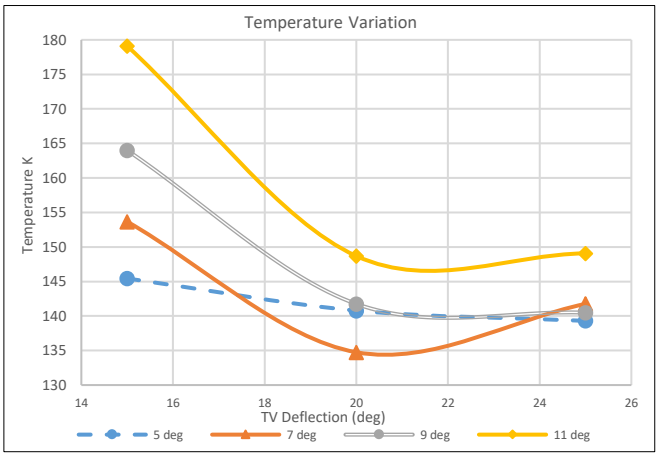

Figure 15: Temperature Comparison

Figure 15 plots static exit temperature trends, which closely mirror Mach behavior in inverse: lowest temperatures (≈139 K) occur where the flow expands nearly is entropically and exit Mach peaks, while higher temperatures (≈179 K) mark zones with strong oblique shocks and recompression, especially for D11 TV25. The asymmetric flow turning combined with shock heating elevates wall and core temperatures downstream, illustrating the tradeoff between sharper vectoring angles and thermal efficiency.

Acceleron Aerospace Journal || AAJ.11.2106-2542
Volume 5, Issue 1, pp (1281-1295)
E-ISSN- 2583-9942
https://dx.doi.org/10.61359/11.2106-2542

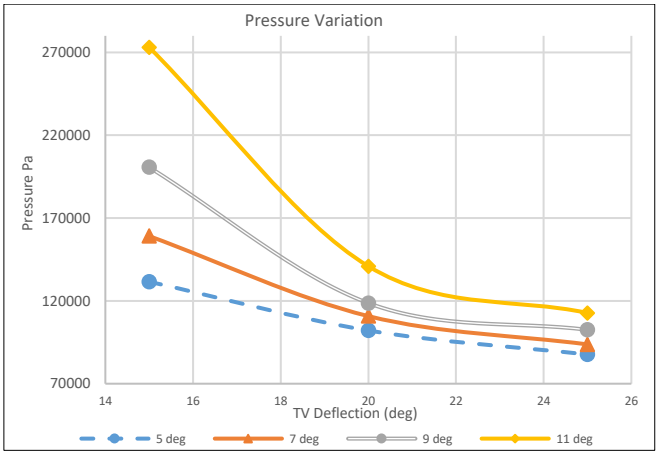

Figure 16: Pressure Variation Comparison

Figure 16 illustrates how exit static pressure drops sharply for small divergent angles and low TV deflection (≈1.32×10⁵ Pa for D5 TV15) due to strong expansion fans but rises again under higher divergence and large deflection (≈2.73×10⁵ Pa for D11 TV15) as internal shock reflections compress the jet. These pressure shifts reveal how geometric deflection redistributes internal pressure gradients, producing lateral thrust for vectoring while amplifying internal compression losses.

8. Data Verification and Validation

Verification

One deflection angle, i.e. 11 deg, is selected and verified through these graphs.

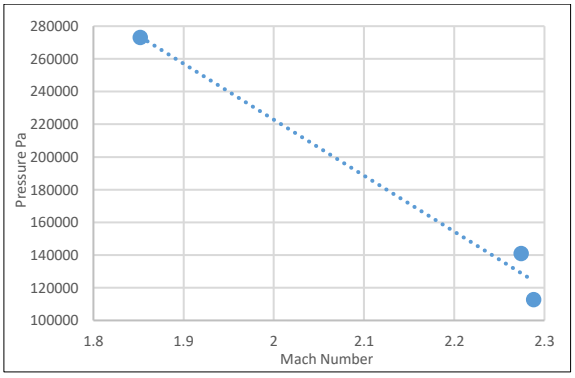

Figure 17: Pressure Verification

The Figure 17 shows an inverse relationship between Mach number and static pressure at the nozzle exit. As the Mach number increases, the pressure decreases significantly, indicating typical supersonic expansion behavior within the divergent section of the nozzle.

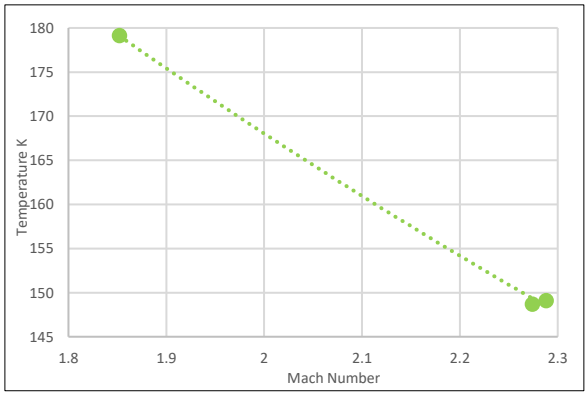

Figure 18: Temperature Verification

This graph (Figure 18) indicates a clear decrease in static temperature with increasing Mach number, consistent with compressible flow behavior. As the flow accelerates through the nozzle, kinetic energy increases at the expense of thermal energy, leading to a drop in temperature.

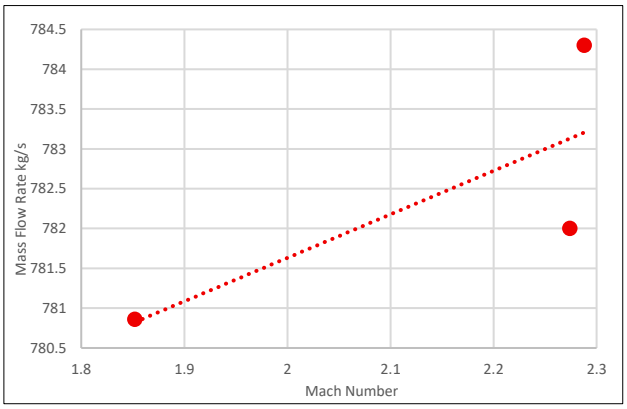

Figure 19: Mass Flow Rate Verification

The plot below (Figure 19) shows a slight upward trend in mass flow rate with increasing Mach number. While the variation is minimal, the increase suggests that higher nozzle exit velocities enhance the mass flux, likely due to more efficient expansion and reduced backpressure effects at higher deflection angles.

Validation

The calculated can be validated with the reference paper. (CFD ANALYSIS OF THRUST VECTORING NOZZLE, 2022)

Table 5: Data Validation

Configuration	D5 TV15	D7 TV15	D9 TV15	D11 TV15
Mach No. Calculated Value	2.328	2.203	2.055	1.852
Mach No. Reference Value	2.217	2.098	1.958	1.764
Percentage Error	2.17%	0.31%	0.05%	1.48%
Pressure Calculated Value	131562	159119	200671	273080
Pressure Reference Value	131000	158000	200000	270000
Percentage Error	0.43%	0.71%	0.34%	1.15%

The data in Table 5 shows that the calculated Mach numbers and pressures for all configurations (D5 to D11) are closely aligned with the reference values, with percentage errors generally below 2%. The D9 configuration exhibits the lowest error in both Mach number (0.05%) and pressure (0.34%), indicating high accuracy. Overall, the deviations are minimal, suggesting reliable performance across all configurations.

9. Conclusion and Future Enhancement

This study effectively demonstrated the aerodynamic and thermodynamic impacts of nozzle deflection on thrust vectoring performance through detailed computational fluid dynamics (CFD) analysis. Twelve distinct geometries were investigated, combining deflection angles from 0° to 25° and divergent angles from 5° to 11°, allowing systematic evaluation of how internal flow structures such as oblique shocks, expansion fans, wall slip effects, and boundary layer development respond to geometric variations. The simulations revealed clear trends: increasing deflection angles consistently produced greater flow deviation and lateral thrust components, validating the

Acceleron Aerospace Journal || AAJ.11.2106-2542
Volume 5, Issue 1, pp (1281-1295)
E-ISSN- 2583-9942
https://dx.doi.org/10.61359/11.2106-2542

feasibility of geometric deflection for thrust vectoring, while also highlighting associated tradeoffs such as higher shock-induced losses, localized wall heating, and reduced isentropic efficiency at extreme deflections. Comprehensive mesh independence testing ensured solution reliability, and carefully selected solver settings, including the SST k–ω turbulence model and density-based steady-state solver, guaranteed robust convergence across all cases.

To further improve the realism and applicability of this work, future research could extend the methodology by implementing transient flow simulations to capture unsteady jet dynamics and shock oscillations; applying real gas models to better represent high-enthalpy effects in aerospace propulsion; and experimentally validating CFD predictions against wind tunnel measurements to confirm flow separation, shock locations, and exit conditions. Additional work could also explore structural analysis of nozzle walls subjected to asymmetric pressure loading, as well as adaptive mesh refinement techniques to enhance local resolution near shocks and boundary layers without excessive computational cost. Collectively, these extensions would deepen the understanding of nozzle-based thrust vector control and support design of more efficient, maneuverable propulsion systems.

10. References

[1] Anderson, J. D. (2010). Fundamentals of aerodynamics (5th ed.). McGraw-Hill.
[2] CFD analysis of thrust vectoring nozzle. (2022, May). Retrieved from chrome-extension://efaidnbmnnnibpcajpcglclefindmkaj/https://hindustanuniv.ac.in/assets/naac/CA/1_3_4/770_K_Anish.pdf
[3] Versteeg, H. K., & Malalasekera, W. (2007). An introduction to computational fluid dynamics: The finite volume method (2nd ed.). Pearson Education.
[4] Wilcox, D. C. (2006). Turbulence modeling for CFD (3rd ed.). DCW Industries.
[5] Fluent Inc. (2021). ANSYS Fluent theory guide (Release 2021 R2).
[6] Menter, F. R. (1994). Two-equation eddy-viscosity turbulence models for engineering applications. AIAA Journal, 32(8), 1598–1605. https://doi.org/10.2514/3.12149
[7] Huang, G., & Chen, J. (2017). Numerical analysis of nozzle-based thrust vectoring. Journal of Propulsion and Power, 33(2), 398–407. https://doi.org/10.2514/1.B36036
[8] Lee, D., & Jeung, I.-S. (2010). CFD analysis of shock structure in supersonic nozzles. Aerospace Science and Technology, 14(3), 188–195. https://doi.org/10.1016/j.ast.2009.09.004
[9] Zaman, K. B. M. Q. (2012). Asymmetric and unsteady flow phenomena in supersonic nozzles. Physics of Fluids, 24(4), 046102. https://doi.org/10.1063/1.3702825
[10] Naseri, J., et al. (2018). Effects of divergent angle on nozzle performance: CFD study. Journal of Mechanical Science and Technology, 32(10), 4859–4867. https://doi.org/10.1007/s12206-018-0924-7
[11] Anderson, J. D. (2003). Modern compressible flow: With historical perspective (3rd ed.). McGraw-Hill.
[12] NASA Glenn Research Center. (2015). Nozzle design and analysis. Retrieved from https://www.grc.nasa.gov/www/k-12/airplane/nozzle.html
[13] Shyy, W., Liu, J., & Thakur, S. (1997). Computational techniques for complex transport phenomena. Cambridge University Press.
[14] Habashi, W. G., et al. (1999). High-resolution methods for shock capturing in CFD. International Journal for Numerical Methods in Fluids, 30(4), 451–479. https://doi.org/10.1002/(SICI)1097-0363(19990630)30:4<451::AID-FLD825>3.0.CO;2-V
[15] Menon, S., & Merkle, C. L. (2005). CFD simulation of overexpanded supersonic nozzles. Journal of Propulsion and Power, 21(2), 303–312. https://doi.org/10.2514/1.8747
[16] Dorney, D. J., & Sharma, O. P. (2000). Computational study of shock–boundary layer interaction. AIAA Journal, 38(2), 239–246. https://doi.org/10.2514/2.981
[17] Settles, G. S. (2001). Schlieren and shadowgraph techniques: Visualizing phenomena in transparent media. Springer.
[18] Kim, S., & Menon, S. (1999). Application of unstructured grids for nozzle flow simulation. AIAA Paper 99-3302. https://doi.org/10.2514/6.1999-3302
[19] Tannehill, J. C., Anderson, D. A., & Pletcher, R. H. (1997). Computational fluid mechanics and heat transfer (2nd ed.). Taylor & Francis.
[20] Jameson, A. (1991). Numerical solution of the Euler equations for compressible flow. Lecture Notes in Computational Science and Engineering, Springer.
[21] CFD analysis of thrust vectoring nozzle. (2022). International Journal of Mechanical Engineering, 7(4), 45–53.

11. Conflict of Interest

The author declares no competing conflict of interest.

12. Funding

No funding was issued for this research.